geotechnics

MDPI

Article

Numerical Studies of the Floor Heave Control Method in Gob-Side Entry Retaining in Deep Coal Mines

Ivan Sakhno [1,*], Svitlana Sakhno [1], Oleksandr Kyrsanov [2], Serhii Bashynskyi [3], Oleksandr Nosach [2], Liubov Shaidetska [4] and Denys Darmostuk [5]

[1] Department of Mining, Mining and Metallurgy Faculty, Technical University "Metinvest Polytechnic" LLC, Pivdenne Shose 80, 69008 Zaporizhzhia, Ukraine; svitlana.sakhno@mipolytech.education
[2] Department of Mineral Deposit Development, Educational and Scientific Institute of Mining and Geoengineering, Donetsk National Technical University, Sambirska Str. 76, 82111 Drogobich, Ukraine
[3] Department of Mining Technologies and Construction Named After Prof. Bakka M.T., Faculty of Mining, Environmental Management and Construction, Zhytomyr Polytechnic State University, Chudnivska Str. 103, 10005 Zhytomyr, Ukraine
[4] Department of Geoengineering, National Technical University of Ukraine "Igor Sikorsky Kyiv Polytechnic Institute", Prospect Beresteiskyi 37, Solomyanskyi District, 03056 Kyiv, Ukraine
[5] Institute for Personnel Training of the State Employment Service, Novovokzalna St. 17, 03038 Kyiv, Ukraine
* Correspondence: ivan.sakhno@mipolytech.education

Abstract

In the case of pillarless coal mining, the floor uplift reaches 60–80% of the total vertical convergence in gob-side entry, while total convergence often exceeds 1.0 m. This is one of the key factors impedimental to pillarless mining in deep coal mines. Traditional methods of floor heave control in gob-side entry are not effective enough, so they need to be improved. This paper is devoted to the improvement of the anti-shear pile method in gob-side entry retaining. Finite element analysis was used as the main study method. The influence of pile diameter and its design on the stress–strain distribution in the surrounding rock and on the floor uplift magnitude was determined. It was found that the filled piles are the most efficient in reducing floor heave magnitude, asymmetry of floor uplift, and size of post-peak strain in the immediate floor. In filled piles, the steel tube prevents the concrete core from fracturing, while the concrete core prevents the steel tube from plastic yielding. Therefore, with the same diameter and elastic modulus, filled piles are 1.06–1.7 times more effective in floor heave control than comparable analogs.

Keywords: floor heave control; pillarless mining; gob-side entry retaining; floor reinforcement; numerical simulation; anti-shear pile method

Check for updates

Academic Editor: George Mylonakis

Received: 1 April 2026
Revised: 3 May 2026
Accepted: 13 May 2026
Published: 15 May 2026

Copyright: © 2026 by the authors. Licensee MDPI, Basel, Switzerland. This article is an open access article distributed under the terms and conditions of the Creative Commons Attribution (CC BY) license.

1. Introduction

In the last decade, pillarless coal-mining technologies have made significant progress, primarily due to the development of the N110 construction method by Professors Song and He [1]. This method is based on directional cutting of the main roof to eliminate the structural connection between the gob roof and the roadway roof, which enables the formation of a short cantilever beam structure in the roof strata above the roadway (Figure 1a) [2]. Undoubtedly, pillarless coal-mining technologies are promising due to their many advantages [3,4]. However, outside of China, the N110 construction method has not found wide application.

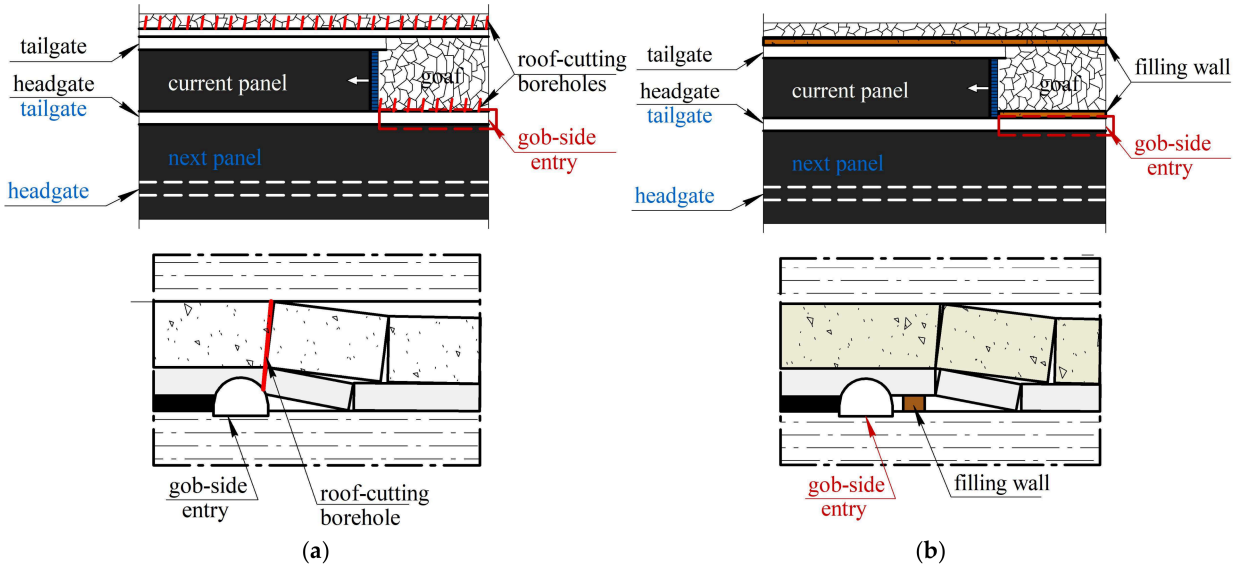


Figure 1. The pillarless coal mining technologies: (**a**) N110 construction method; (**b**) pillarless method with filling walls.

In Europe, pillarless coal mining technologies are currently primarily associated with the use of filling walls made of quick-setting materials (Figure 1b). A filling wall is an artificial structure designed to support the roof after the coal seam has been extracted. Wall bodies compensate for the coal seam, so prompt roof support after excavation is crucial to the effectiveness of filling walls. Until the mid-20th century, wooden cribs were typically used for gob-side entry retaining; later, concrete blocks and phosphogypsum filling walls were used. Nowadays, rapid-hardening concrete, paste-like backfill material, and high-water packing material are predominantly used. Many scientists have studied the efficiency of the filling wall body of gob-side entry retaining in fully mechanized longwalls [5,6]. In Ukraine, where primarily thin coal seams are excavated, pillarless technologies with filling walls made of rapid-hardening concrete materials turned out to be the most effective ones [7]. The main restraining factor for the widespread use of pillarless technologies is the difficulty of ensuring the stability of the gob-side entry [8]. The floor uplift reaches 60–80% of the total vertical convergence in gob-side entry. This is explained by the fact that the roof and wall sides are typically supported by U-shaped steel arches, rock bolts, cable bolts, and energy-absorbing bolts [9], while reinforcement is usually not used in the entry's floor. The problem of floor heave is especially acute for deep coal mines and entries in soft rock.

Traditional concepts of floor heave mechanisms were described by Faria Santos and Bieniawski [10]. These three main mechanisms are bearing capacity failure, buckling, and swelling. However, in the gob-side entry of deep mines, these mechanisms are complicated. Therefore, many scientists have studied the floor heave mechanism in gob-side entry retaining using numerical simulation, physical modeling, and in situ monitoring [11–14].

Gong et al. [11] showed that the horizontal stress in the roadway's floor is the external factor that directly causes floor heave in the roadway. Other external factors affect the failure characteristics of the roadway's floor by changing the horizontal stress of the floor in the roadway. Li et al. [12] believed that the floor heave of entry retaining was caused by high vertical stress in the solid coal from one side and in the filling body from the other side. The floor was squeezed by two sides to form an asymmetric sliding force towards the entry span. Yu et al. [13] also believed that the vertical pressure on the filling body and on the coal seam is the main cause of heaving, which allowed them to propose a method of floor heave control based on pressure relief by roof cutting. The increase in the caving height of the immediate roof in the goaf reduces the subsidence amount of the main roof and thus

decreases the abutment pressure on the coal sides. The authors [12,13] did not directly indicate the role of horizontal stresses, but without a change in the horizontal stresses, it is difficult to explain the transformation of the floor squeezing in the sides of the entry to vertical expansion with delamination below the entry span. Lin et al. [14] believed that the floor heave in the entry retaining of deep swelling soft rock occurs due to the transfer of the "compression mold effect" in the backfilling body and solid coal, horizontal pressure generated by main roof rotation, compaction of caving roof in the gob, deep high stress, and soft rock swelling pressure. Sun et al. [15] found the dangerous location of asymmetric floor heave in the entry and showed that the horizontal stress had a great effect on the floor heave failure.

Certain conditions must be met so the surrounding rocks can move and the vertical stresses in the sides of the entry can transform into lamination and uplift of rock within the entry span. For dry rock mass, this is usually failure, and for wet rock mass—plastic flow [16]. Post-peak stress and strain are indicators of the risk factor of floor uplift. Most scientists believe that the magnitude of floor uplift depends on the vertical–horizontal stress ratio [17–19]. Zhang and Shimada [19] directly postulate that variations in the horizontal–vertical stress ratio in the floor strata are the main cause of large floor heave. Mo et al. [20] proposed Coal Mine Floor Rating as a new rock mass classification system for the coal mine floor. This rating takes into account both the degree of discontinuity and the magnitude of horizontal stress. Clearly, the effectiveness of floor heave control depends on the degree of influence on the heaving mechanism. Effective floor heave control methods are based on control of this mechanism. Therefore, understanding the characteristics of floor heave evolution is essential for choosing a control method. Although the problem of floor heave evolution has been well studied, floor stability remains a challenge under the aforementioned conditions, and further research is needed.

To increase the effectiveness of traditional floor reinforcement methods such as rock bolts, grouting [21], stress relief [22], inverted arch system [23], combined methods have been widely used [24,25]. Such methods, despite the achieved practical results, do not imply new ideas of impact on rock mass that differ from traditional reinforcing or destressing. However, recently, two new methods of floor heave control have been developed: the roof-cutting method and the anti-shear pile method. These methods take into account the peculiarities of the evolution of floor heaves in gob side entry.

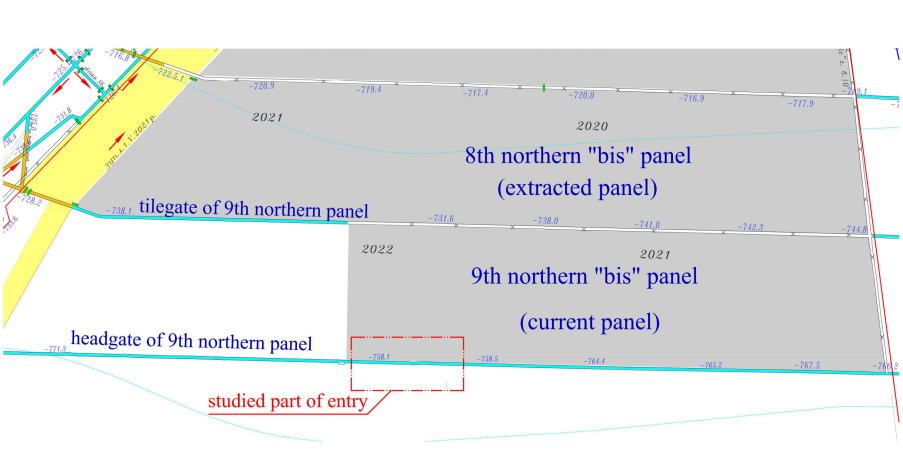
Gai et al. [26] developed the idea that Professor He Manchao [1] first introduced, which is a new type of roof-cutting technology and gob-side entry retaining to reduce mining disturbance of the floor and study failure characteristics along strike direction. A similar roof-cutting solution is also proposed by Qin et al. [27]. In the study [27], the roof-cutting pressure-relief scheme was optimized with the aim of relieving and re-routing the asymmetrically transmitted pillar loading. The optimal roof-cutting length and angle were proposed, which restored a more symmetric stress field and reduced the stress peak, leading to the floor heave decreasing. Sakhno et al. [28] studied floor heave control with an anti-shear pile method. This study improved the idea of Xu et al. [29], which proposed installing steel piles in entry floor corners in front of the dynamic pressure zone. However, unlike Xu et al. [29], Kang et al. [30], and Guo et al. [31], who proposed to install piles in entry corners, Sakhno et al. [28] established the optimal pile installation scheme in the entry span and the optimal pile length. It was found that the anti-shear piles restrain the transformation of high vertical stresses in the entry floor underneath the filling wall and coal seam body into horizontal stresses. As a result, the floor heave magnitude and the size of the zone of horizontal post-peak strain significantly reduce. An unresolved area of the anti-shear pile method is the influence of the pile type and pile diameter on the floor heave and stress–strain state.

Nowadays, specialized software such as FLAC3D, Phase2/RS2, and UDEC is successfully used for numerical simulation of rock mass behavior, including the post-peak stage. However, for cases concerning the analysis of the influence of various elements of support systems (U-shaped steel arches, rock bolts, anchors, steel mesh, piles, etc.) on the stress–strain state, these software have limitations, which often lead to excessive simplifications of models in practice. In contrast, ANSYS solves this problem quite successfully [28,32–37]. Input of adequate initial data of rock mass (for example, that considers the Hoek-Brown criteria) allows stress–strain analysis with complex geometry and various support system elements with high accuracy. Since this study involves analyzing the influence of anti-shear pile parameters on the stress–strain state of surrounding rocks and floor heave, ANSYS code was chosen for this study.

This paper is devoted to the improvement of the anti-shear pile method in gob-side entry retaining and to the elimination of the aforementioned gaps. The main novelty of this paper is the study of the influence of pile diameter and design on the stress–strain distribution in the surrounding rock and floor uplift magnitude. Numerical simulation with ANSYS (version 17.2) code was used for the stress–strain analysis of the surrounding rock. Based on this analysis, the most effective parameters of the anti-shear pile method were determined.

2. Engineering Background

The Pokrovske mine is the largest underground coal mine in Ukraine, with a production capacity of up to 6 million tons of coal per year. The mine has conditions typical of the Ukrainian Donbas. The coal seam thickness is 0.8–2.0 m, and its depth is 800–1000 m, with an average inclination of 2–5°. The studied section of the mine field is located in block 10. The 9th northern "bis" panels have advanced Y-type longwall mining systems (Figure 2a) based on a retained gob-side entry. In Y-shaped systems, fresh air can flow in through two entries before the coal face and then flow out through gob-side entry retaining. When the longwall panel is mined out, gob-side entry retaining can be reused for the next longwall panel.



(a)

Column	Lithology	Thickness (m)	Uniaxial compressive strength σ_c, (MPa)
	sandstone	22	σ_c=44 MPa
	siltstone	10	σ_c=37 MPa
	coal seam	0.8-1.3	σ_c=13 MPa
	siltstone	7.7	σ_c=38 MPa
	sandstone	24.0	σ_c=59 MPa

(b)

Figure 2. The geological and engineering conditions of a longwall panel: (**a**) layout of longwall panels; (**b**) strata histogram.

The seam thickness within the panel varied from 0.8 to 1.3 m. The immediate roof and immediate floor of the seam consisted of siltstone. The main roof and main floor consisted of sandstone. The strata histogram is shown in Figure 2b. Coal extraction was carried

out with floor undercutting to a thickness of 1.15–1.50 m. The average seam thickness, considering the floor undercutting, was 1.3 m.

At the 9th northern "bis" headgate of block 10, a U-shaped steel arch frame KShPU-M-20.3 (U33) with steel mesh was used as the main support. Five full resin rock bolts, 2.4 m long, were also installed in the roof of the entry with a spacing of 1.0 m × 1.0 m. The designed cross-section of the entry was 20.3 m^2. The width and height of the entry during excavation were 6.00 m and 4.63 m, respectively. The distance between the steel arch frames was 0.50 m. Rock bolts were installed between rows of frames in odd rows. The entry was supported by a 1.20 m wide filling wall made of quick-hardening "Bi-Krep" material. Figure 3a,b shows the original design of the support scheme at the stage of entry development and maintenance, respectively. At a retreat length of 25 m, the total vertical convergence was approximately 33% of the initial entry height. Floor uplift accounted for 78% of the vertical convergence (1.2 m), and roof subsidence accounted for 22% (0.33 m). The support frames of the headgate deformed asymmetrically. The steel arches were critically bent and irreversibly deformed. Floor dinting was carried out by a Hasemag EL160 loader (HAZEMAG & EPR GmbH, Dülmen, Germany) (Figure 3c). The entry's height after dinting was 4.3 m. The dinting depth was 1.2 m. The rocks of the immediate roof at the dinting face were highly fractured, with delamination parallel to the bedding planes. (Figure 3d).

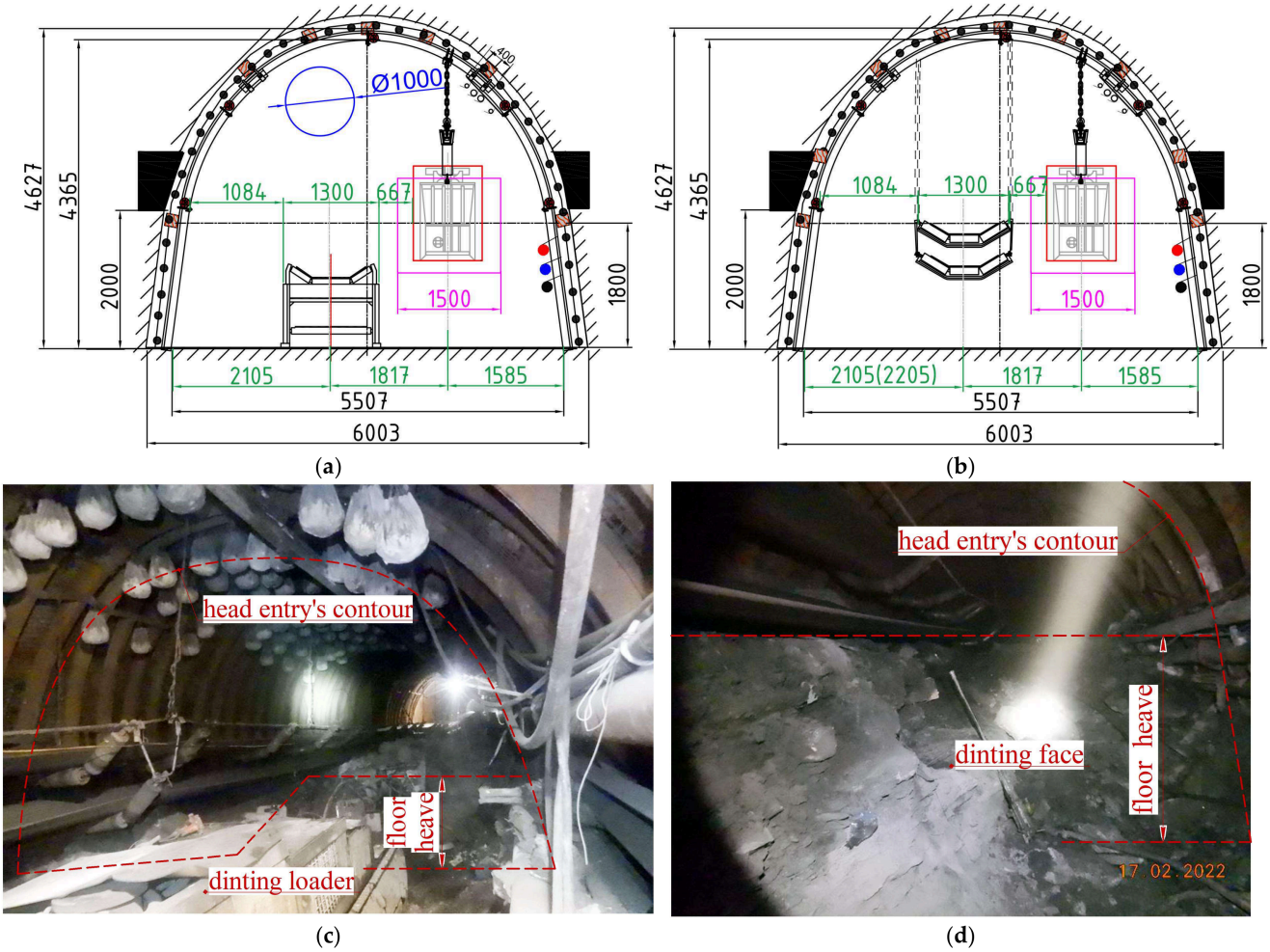


Figure 3. The support system of headgate: (**a**) design of the support scheme on the stage of entry development; (**b**) design of the support scheme on the stage of entry maintenance; (**c**) view on gob-side entry during floor dinting; (**d**) view on floor dinting face.

3. Laboratory Tests

The object of the study is floor heave, and the subject of the study is the immediate floor. Therefore, for laboratory testing, siltstone specimens were picked from the dinting face.

Siltstone specimens picked in the mine were wrapped in stretch film to preserve their natural moisture content. Then, in the laboratory, using a stone-cutting machine, the specimens were cut without a water supply. This allowed to preserve the siltstone's natural moisture content. The specimens were rectangular parallelepipeds with a 70 mm square base. The height of the specimens was 100 mm. The average weight of the specimens was 1.15 kg. The parallelism of the specimens' edges was controlled; the permissible deviation was 0.1 mm. Specimens for testing were rejected if their mass deviation exceeded ±5%. Five specimens were selected for strength testing in natural moisture conditions. One specimen was used to determine the natural moisture content. After drying this specimen, the dry strength of the siltstone was determined. Figure 4a shows the equipment used during the specimen preparation stage.



(**a**) (**b**)

Figure 4. Laboratory equipment: (**a**) preparatory stage equipment; (**b**) compression testing machine.

In addition, laboratory tests were carried out on specimens of filling wall material ("Bi-Krep"). These specimens were prepared by mixing the "Bi-Krep" mixture with water. The water-cement ratio was 0.5. Filling material was poured into 70 × 70 × 70 mm metal molds and air-dried for 28 days. Afterward, the specimens were checked for parallelism and prepared for testing. The average weight of the specimens was 0.74 kg. The parallelism of the specimen edges was checked; the permissible deviation was 0.07 mm. Test specimens were rejected if their mass deviation exceeded ±5%. Five specimens were selected for testing.

The natural moisture content of rock was defined as the ratio of the weight of water to the weight of rock matrix, expressed as a percentage. The specimens were dried in a drying oven at 110 °C until their weight ceased to change during drying. The specimens' weight was monitored every 15 min. The moisture content curve for the specimen during drying is shown in Figure 5a. After 180 min, the specimen stopped losing weight. The natural moisture content of the siltstone was 0.91%. The very low moisture content of the specimen suggests that water was not a significant factor in the floor heave. This establishes a basis for disregarding the moisture factor in subsequent studies.

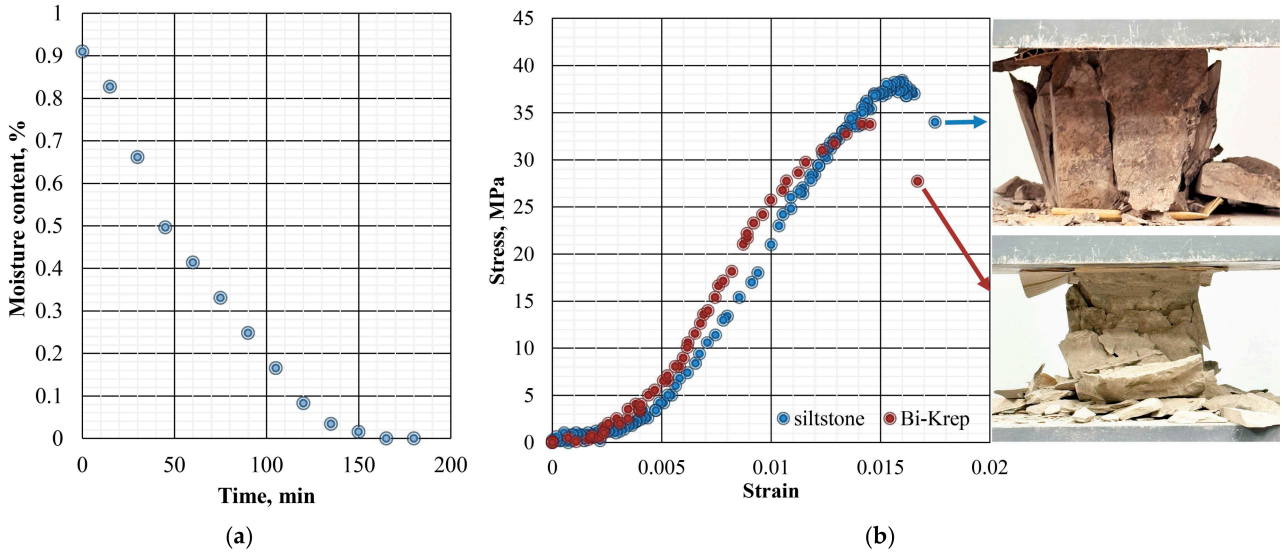


Figure 5. Laboratory test results: (**a**) variation in the specimens' moisture content during drying; (**b**) stress–strain curves for specimens of siltstone and filling wall material.

The uniaxial compressive strength (UCS) of the specimens was determined by an automatic compression testing machine (Figure 4b). The test results for five specimens were averaged to obtain a universal characteristic. The range of values of the UCS test results did not exceed 10%. The test results are shown in Figure 5b as stress–strain curves, and in Table 1. Then, for siltstone and filling wall material specimens, the average deformation modulus was calculated for the stress range 20–100% of the UCS. On the section of the curve taken for analysis (20–100% of the UCS), the calculation of the deformation modulus was performed between every two adjacent loading steps by dividing the increase in vertical stress by the increase in longitudinal strain. Then the arithmetic mean of these values was found. This value is indicated in Table 1 as the average deformation modulus. To determine the Poisson's ratio, a separate experiment was conducted with specimens loaded to 75% of the UCS. The Poisson's ratio was defined as the ratio of the average transverse strain to the longitudinal strain. The average transverse strains were determined as the arithmetic mean between the strains in two mutually perpendicular directions. The test results and calculated values of the average deformation modulus are presented in Table 1.

Table 1. Test results.

Material	Density, (kg/m^3)	UCS, (MPa)	Average Deformation Modulus, (GPa)	Poisson's Ratio
Siltstone (from dinting face)	2356	38.40	3.506	0.27
Material of filling wall	2170	33.78	3.652	0.23

The results of the laboratory tests were used in the next step of the study–numerical simulation.

An analysis of the specimen's stress–strain curves (Figure 5b) shows that both stress–strain curves represent the typical four stages of specimen loading. The first stage involves preliminary compression of the specimen, crack closure, and compensation of surface irregularities. This stage is characterized by a concave section of the curve. Then, in the second stage, a nearly linear increase in stress and strain occurs. The third stage is characterized by a decrease in the inclination angle of the stress–strain curve near the UCS.

Minor pseudo-plastic deformations are observed at this stage. Finally, the fourth post-peak stage is characterized by a decrease in stress beyond the ultimate strength.

Siltstone has the highest UCS and the lowest average deformation modulus. Moreover, at the second stage of loading, the siltstone's deformation curve demonstrates a linear elastic behavior. The behavior of the filling material is characterized by distinct areas of plastic deformation. Although the average deformation moduli of the specimen differ slightly, the variations in deformation modulus for siltstone are less significant (3.000–3.884 GPa) than for Bi-Krep (2.100–4.08 GPa). The fracture patterns of the specimens also vary (Figure 5b). The siltstone is characterized by brittle fracture with large fragments, while the filling material demonstrates small-piece fracture with flake-like fragments.

4. Numerical Simulation

The ANSYS software was used to study the stress–strain evolution of the surrounding rock and support system. The rock mass, filling wall material, concrete pile material, and broken gangue in the goaf were simulated with the Drucker-Prager model. The Drucker-Prager model has been repeatedly used for the simulation of the coal mine roadway stability, both in previous studies of the authors [28,37] and in studies of other scientists [38–44]. The bilinear isotropic hardening model was used to simulate the U-shaped steel-arch and tube-pile.

The numerical model was designed according to the geological strata of the 9th northern "bis" panel of block 10 (Figure 2). A 6.0 × 4.7 m arch-shaped frame KShPU-M-20.3 was simulated. The beam element with a hat-like cross-section was used to simulate the U-shaped steel arch. The position of the coal seam in the entry section was taken from mining practice (Figure 6). The filling wall's width was 1.4 m, and the horizontal distance between the wall and the arch frame was 0.6 m. The distances between steel arch frames were 0.50 m, as at the 9th northern "bis" head entry in situ. The model was 65 × 65 × 65 m (Figure 5). Vertical displacement of the model was fixed at the bottom boundary. The displacements of lateral boundaries were constrained in the normal direction. A vertical pressure of 20 MPa was applied to the top of the model. This pressure was equivalent to the strata weight at the depth of 800 m.

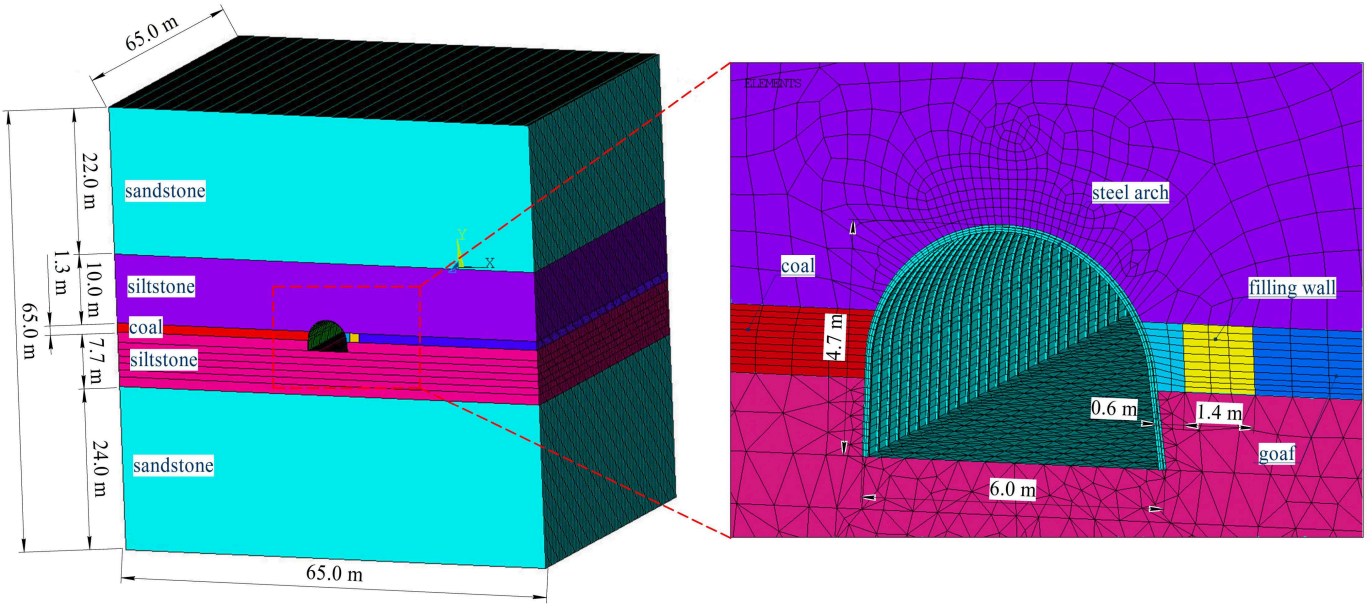


Figure 6. Numerical model.

A meshing of tetrahedron and hexahedron elements was used in the model. The main part of the model was divided into hexahedra, since this ensures high accuracy with a smaller number of elements. The more complex geometry of the entry's floor, as well as the presence of piles, led to the use of tetrahedron elements in the immediate floor. The numerical model was automatically divided into finite elements by the built-in meshing module. Subsequently, a manual mesh optimization was performed to achieve a more accurate analysis near the entry's floor. After mesh generation, the model was checked for geometric errors (such as zero-length elements, degenerated elements, and duplicate node numbers). Before the main simulation stage, a sensitivity analysis of the model was conducted to optimize the size of the finite element mesh. To solve the test model, a series of identical calculations were performed, in which only the mesh size varied (all other data were equal). The optimization criterion was the floor heave.

The initial data for rock modeling were taken from the geological survey. The properties of the main roof, immediate roof, and floor were determined from core testing (Figure 2b). The properties of the immediate floor and filling wall material were determined according to the results of laboratory tests presented above (Table 1).

Since the surrounding rocks were fractured, the parameters of intact rock were corrected to correspond to rock mass parameters. Hoek-Brown Failure Criterion [45] was used to calculate the properties of the rock mass. Hoek-Brown Parameters: the Geological Strength Index (GSI), values of the constant mi, and the Disturbance factor (D) were determined. The GSI was calculated from the RMR index (GSI = RMR89 − 5) [46] that based on the results of uniaxial strength tests, the examination of the drill cores, and the observation of rock in the entry. The RMR parameters were determined [47]: strength of intact rock, RQD, spacing of discontinuities, condition of discontinuities, groundwater conditions, effect of discontinuity strike and dip orientation on drivage. Hoek and Diederich's empirical method [46] was used to calculate the deformation modulus, angle of friction, and cohesive strength of rock mass. The calculation method is described in more detail in [16,37].

The properties of rock mass and filling wall material are shown in Table 2. Mechanical parameters of the U-shaped steel arch and tube-pile are shown in Table 3.

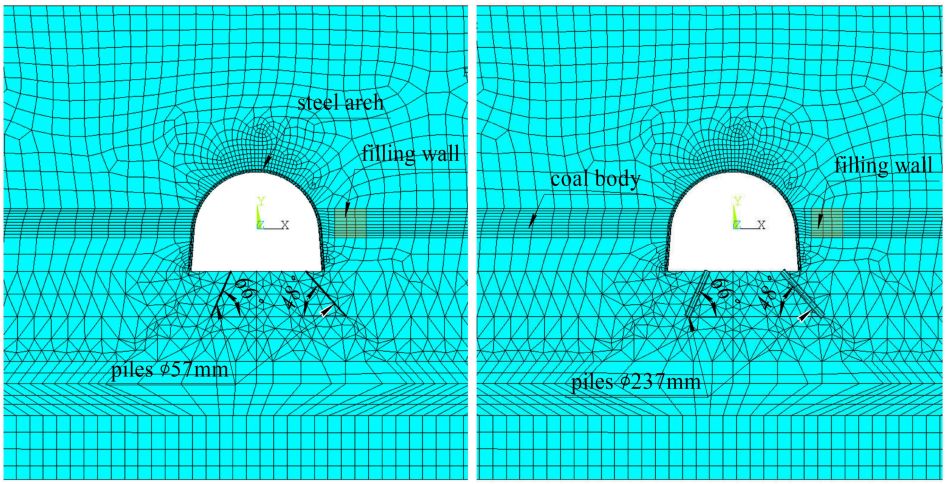
Table 2. Intact rock properties and calculated rock mass properties.

Rock Strata	Intact Rock			GSI/D/m	Rock Mass		
	Density (kg/m^3)	Deformation Modulus (MPa)	Compressive Strength (MPa)		Deformation Modulus (MPa)	Compressive Strength (MPa)	Tensile Strength (MPa)
Main roof (Sandstone)	2400	7100	44.0	57/0.5/8	1625	2.47	0.14
Immediate roof (Siltstone)	2400	5800	37.0	56/0.5/8	1250	1.94	0.11
Coal	1350	1970	13.0	35/0/17	224	0.32	0.007
Immediate floor (Siltstone)	2356	3506	38,40	49/0.5/8	484	1.24	0.06
Main floor (Sandstone)	2400	8050	59.0	67/0.5/12	3111	6.50	0.30
Filling wall material (Bi-Krep)	2170	3652	33.78	84/0.5/12	2310	8.65	0.72

Table 3. Properties of support elements used in the model.

Primary Support	Type of Elements	Material Behavior Option	Elastic Modulus (GPa)	Poisson's Ratio	Yield Strength (MPa)	Tangent Modulus (GPa)
U-shaped steel arch	Beam	Bilinear isotropic hardening	200	0.27	295	52.2
Tube (steel 20)	Beam	Bilinear isotropic hardening	200	0.27	220	30

The study had three steps. The first step involved analysis of the floor heave and stress–strain state in the surrounding rocks of the gob side entry without floor reinforcing. In the second step, the analysis was conducted after installation of two piles in the entry's floor using a 2-pile 5 + 2 scheme. The influence of pile diameter on stress and strain was studied. The design and parameters of the support scheme were adopted in accordance with the study of Sakhno et al. [28]. The piles installation step was equal to the installation step of the steel arch frame. Three types of piles were studied: concrete piles, tube-piles, and filled piles. The pile diameter varied between 57 and 273 mm. The pile diameters corresponded to the standard series specified by DSTU 8943:2019 [36]. The floor heave control scheme is shown in Figure 7.



(**a**) (**b**)

Figure 7. Finite-element models of 2 pile 5 + 2 floor heave control scheme with min (**a**) and max (**b**) pile diameters.

The tube-piles consisted of sections of metal tubes fixed in boreholes with concrete mix. However, in the numerical model, simplification was applied, whereby the concrete layer between the borehole walls and the tube was not modeled. The properties and parameters of the tube-piles were also adopted based on the properties of tubes in DSTU 8943:2019 [48]. The concrete piles were simulated as filling wall material poured into boreholes. The filled piles were simulated as tube-piles with concrete filling. This increased the piles' elastic modulus and load-bearing capacity, making them the highest among the compared piles. The bilinear isotropic hardening model (Table 3) was used to simulate the tube-piles. To simulate concrete piles, the Drucker-Prager model and the properties of the filling wall material were used (Table 2). To simulate filled piles, the bilinear isotropic hardening model was used. In this case, the pile was a solid circular beam, not a tube. The filled

pile's modulus of elasticity was calculated as the weighted average modulus of steel and concrete, considering the volume ratio of these materials. This approach is widely used in the calculation of composite structures. The yield modulus and tangential modulus values of filled piles were equal to the corresponding moduli of steel 20 from which the tubes were made. Table 4 shows the properties and parameters of the piles that were modeled.

Table 4. Properties of pile.

Type of Pile	External Diameter, m	Internal Diameter, m	Elastic Modulus of Steel (GPa)	Elastic Modulus of Concrete (GPa)	Weighted Average Elastic Modulus (GPa)
Tube-pile	0.273	0.257	200	-	-
	0.219	0.203	200	-	-
	0.159	0.147	200	-	-
	0.133	0.124	200	-	-
	0.108	0.1	200	-	-
	0.089	0.081	200	-	-
	0.076	0.068	200	-	-
	0.057	0.005	200	-	-
Concrete pile	0.273	-	-	23.1	-
	0.219	-	-	23.1	-
	0.159	-	-	23.1	-
	0.133	-	-	23.1	-
	0.108	-	-	23.1	-
	0.089	-	-	23.1	-
	0.076	-	-	23.1	-
	0.057	-	-	23.1	-
Filled pile	0.273	0.257	200	41	59
	0.219	0.203	200	41	63.4
	0.159	0.147	200	41	64.1
	0.133	0.124	200	41	61.8
	0.108	0.1	200	41	63.7
	0.089	0.081	200	41	68.3
	0.076	0.068	200	41	72
	0.057	0.005	200	41	82

In the third step, the influence of the elastic modulus of the pile on the floor heave and stress–strain state of the surrounding rocks was investigated. At the same time, two types of piles were studied—concrete piles and filled piles. Different behavior options of pile's material were taken into account by applying different models—the Drucker-Prager model for concrete piles and the Bilinear isotropic hardening model for filled piles.

5. Results

5.1. First Simulation Step

The distribution of principal stress and horizontal and vertical strain in the surrounding rocks is shown in Figure 8. Figure 8a shows the distribution of the minimum (σ_3) principal stress. Lithological stresses that correspond to the mining depth are 20 MPa. The stress scale is adjusted to identify zones of increased and decreased stress in the surrounding rocks. Zones of increased stress occur on the sides of the entry, while zones of decreased stress occur in the entry's floor. This pattern corresponds to the traditional concept of a "butterfly zone" (Figure 8a). The zone of increased stress in the roof from the coal body side is larger than the zone of increased stress from the filling wall side. Although the filling wall is more rigid than a coal body, it has limited dimensions. The filling wall tends to deform and be indented into the immediate floor, which causes an increase in the concentration of vertical stress below it. The initial position of the rock strata is shown in Figure 8a,b by the red dashed line. Specific directions of rock strata displacements are marked by arrows in Figure 8a. The red dots in Figure 8a are located at the intersections of the initial position of the rock strata and the position of the rock strata after the coal seam excavation. The lines that connect these dots separate the area of rocks without displacement, the area of rocks with uplift, and the area of rocks with subsidence (Figure 8a).

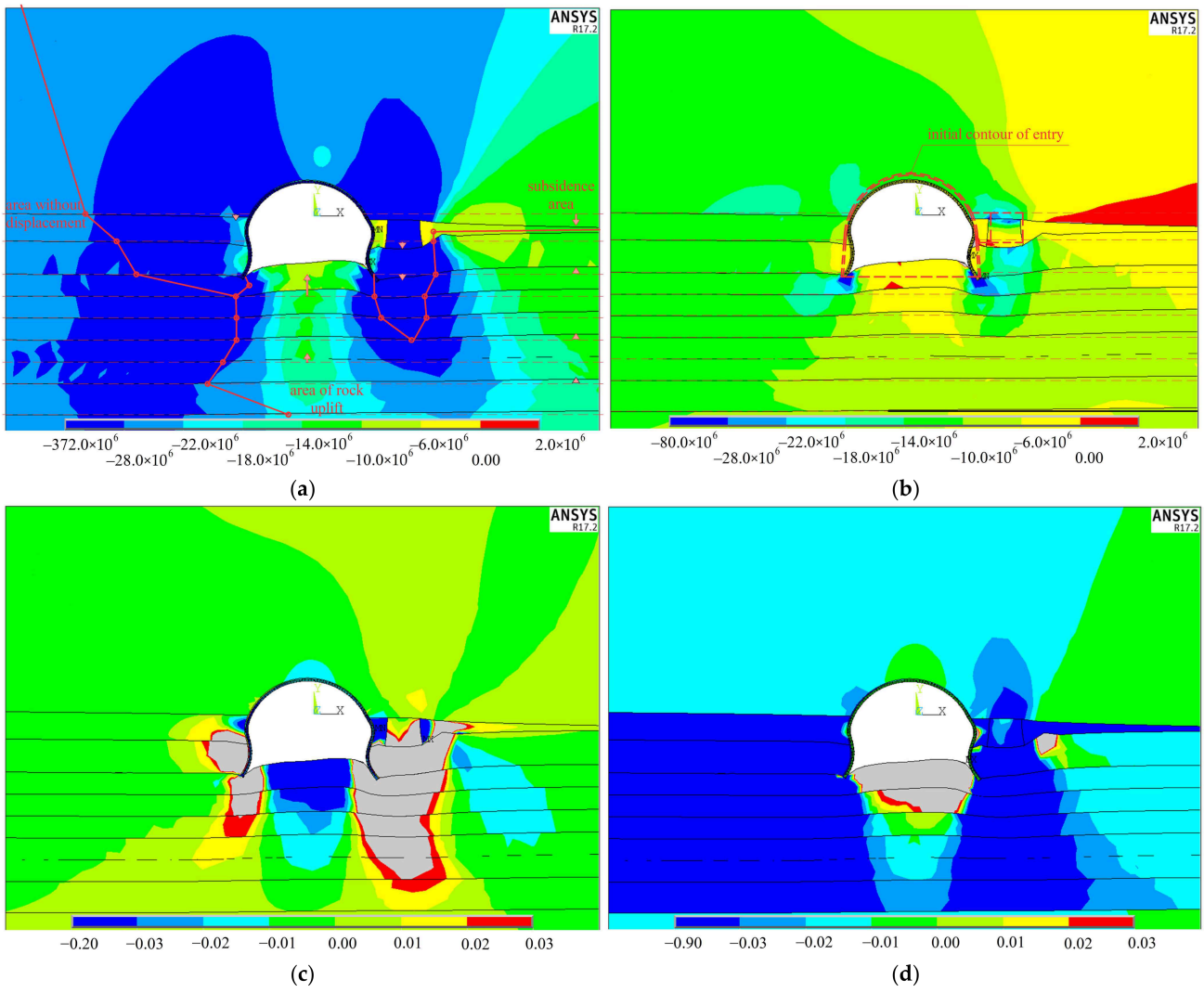


Figure 8. The distribution of minimum (σ_3) principal stress (Pa) (**a**); maximum (σ_1) principal stress (Pa) (**b**); horizontal strain (**c**); vertical strain around the gob side entry (**d**).

In Figure 8b, the red dashed line shows the initial entry contour. The asymmetric deformation of entry and asymmetric floor uplift can be seen by comparing the contours before and after deformation. The steel arch frame deforms unevenly. At the same time, the arch frame legs bend inward toward the entry. The floor uplift from the filling wall side is greater than from the coal body side, which corresponds to the in situ deformations of the entry. Zones of pre-peak tensile stress occur near the entry's walls and the immediate floor.

The maximum floor heave in the model is 0.9 m, while the in situ floor dinting is 1.2 m. The stated floor dinting value is not an exact value and varies along the length of the entry. However, it should be noted that the gob-side entry was studied, so the floor dinting includes both the floor heave and the layer of rock and coal that has fallen onto the entry floor during the entry's existence. Unfortunately, no floor benchmark points were established in this study due to the difficulty of saving them due to the presence of conveyors and other equipment on the entry's floor, which moved with the face. Convergence was determined by measuring the distance to the floor contour. Visual monitoring of the dinting face indicates that the average thickness of the rock and coal layer that has fallen is 0.2 m. Therefore, the error in predicting floor uplift in the model is approximately 10%.

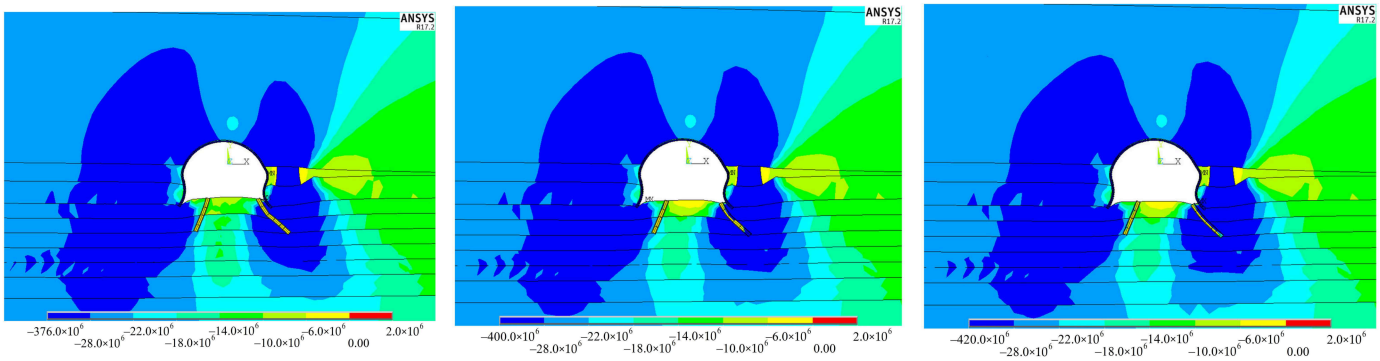
Figure 8c,d provides an opportunity to analyze the strains in the immediate floor. The strain scale is adjusted to clearly show the post-peak strain area, as well as compressive and tensile strains. The failure criterion for strain is applied in the range of "−0.03"–"+0.03", according to the laboratory tests of mudstone, siltstone, argillite [49–51]. The post-peak tensile strain zone is highlighted in gray, and the post-peak compressive strain zone is highlighted in dark blue.

In the entry's floor below the frame's support leg, from the side of the filling wall and from the side of the coal body, zones of increased compressive stresses are formed, oriented in a direction close to vertical (Figure 8a). In these zones, as well as in the zone below the filling wall, horizontal tensile post-peak strains are formed (Figure 8c). From the filling wall side, the zone of tensile horizontal post-peak strains formed below the support's leg merges with the same zone formed below the filling wall. The depth of the post-peak strain zone from the coal body side reaches 2.0 m, and from the filling wall side—5.0 m. Between these zones of horizontal tensile post-peak strains, a zone of horizontal compressive post-peak strains occurs. In this zone, the maximum principal stresses decrease (Figure 8b), and the vertical strains are tensile (Figure 8d). Thus, a zone of post-peak vertical tensile strains is formed below the entry's span (Figure 8d). The immediate floor in this zone expands vertically as a result of horizontal compression and dilatancy. A key role in floor heave is played by the transformation of high vertical stresses and vertical compressive strains below the filling wall and coal body into high horizontal stresses, and strains below the support legs and subsequent transformation into vertical tensile strains below the entry span. In this paper, it is proposed to control the floor heave by restricting the above-mentioned transformations in the immediate floor with anti-shear piles.

5.2. Second Simulation Step

Figure 9 shows the distribution of the minimum (σ_3) principal stress after floor reinforcement by different pile types. Since the greatest effect is observed with the largest pile diameter, Figure 9 shows piles with a maximal diameter (273 mm). Analysis shows that pile installation does not significantly affect the distribution of minimum principal stresses. A slight difference in the stress distribution patterns for different pile types consists of an increase in the size of the high-stress zone in the roof above the filling wall for filled piles (Figure 9c) and tube-piles (Figure 9b) compared to concrete piles (Figure 9a). This is explained by the greater rigidity of the filling wall base in these cases. Visually, the concrete

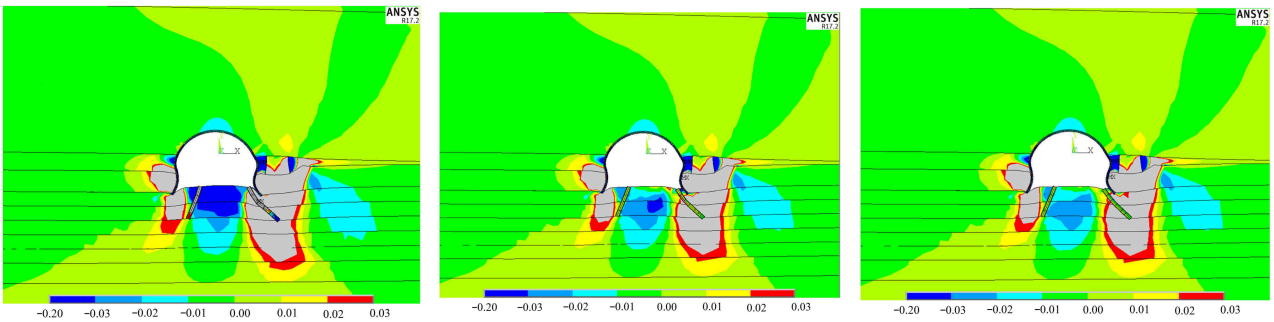
pile deforms more significantly than the other two piles. Moreover, the stress relief zone for the concrete pile is approximately half a meter deeper than for the other variants.



(**a**) (**b**) (**c**)

Figure 9. Minimum (σ_3) principal stress (Pa) distribution around the entry: (**a**) concrete piles; (**b**) tube-piles; (**c**) filled piles.

Figure 10 shows the distribution of horizontal strain after floor reinforcement by different types of 273 mm diameter piles. Pile installation affects the distribution of horizontal strain primarily in the area between the piles. The horizontal tensile strains below the arch frame legs and below the filling wall do not change significantly after pile installation. Below the entry span, post-peak horizontal strains decrease after pile installation. Concrete piles have minimal impact. The strain cloud diagram for this type of pile (Figure 10a) is almost identical to the case without pile installation (Figure 8c). Tube-piles (Figure 10b) reduce the zone of horizontal post-peak strain between piles by 6.5 times. After the installation of filled piles, horizontal post-peak strain below the entry span does not occur (Figure 10c). Thus, it can be concluded that the piles restrict the transfer of horizontal strain in the immediate floor from the sides of the entry to its center. Filled piles show the best effect.



(**a**) (**b**) (**c**)

Figure 10. Horizontal strain distribution around the entry: (**a**) concrete piles; (**b**) tube-piles; (**c**) filled pile.

Figure 11 shows the distribution of vertical strain after floor reinforcement by different types of 273 mm diameter piles. Pile installation has a significant impact on the distribution of vertical strain below the entry span. The size of the post-peak strain zone decreases slightly after installation of concrete piles (Figure 11a) compared to the case without reinforcement (Figure 8d). The floor's contour becomes more symmetrical. Tube-piles prevent the formation of post-peak strains between piles (Figure 11b). Filled piles not only eliminate post-peak strains between piles but also reduce the zone of tensile post-peak strains, indicating stabilization of the stress-strain state of the immediate floor after

reinforcement (Figure 11c). Thus, the piles reduce vertical tensile strains below the entry span, which leads to a decrease in the floor heave.

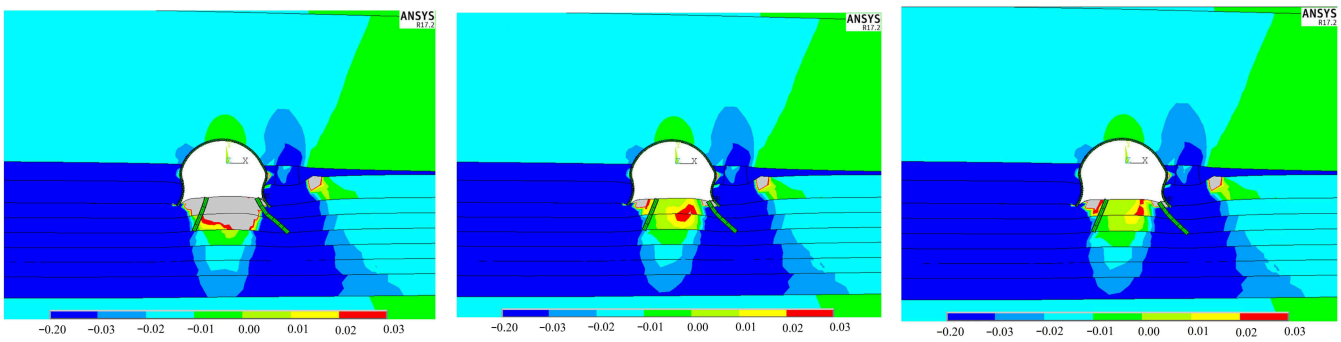
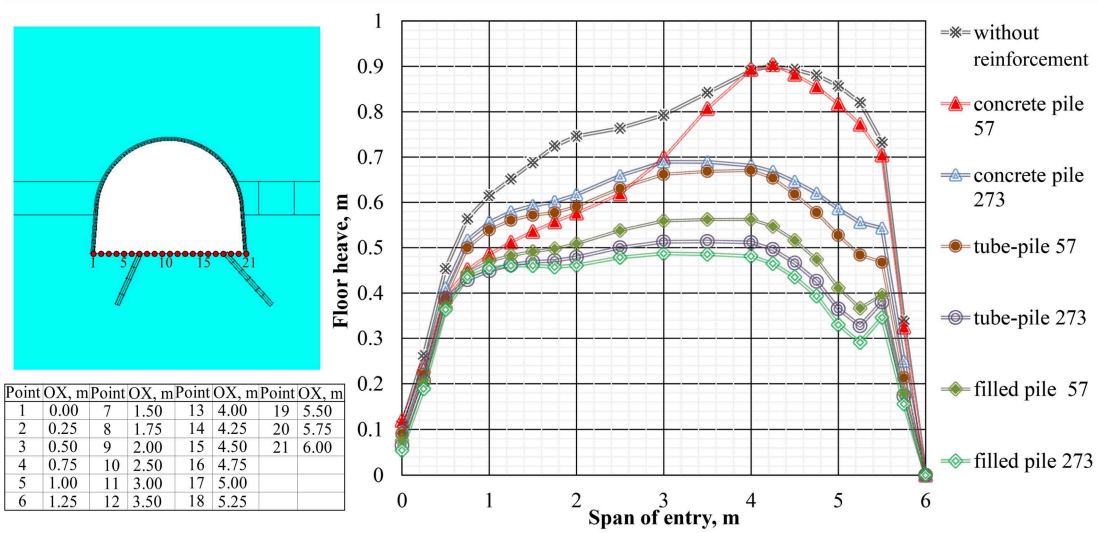


Figure 11. Vertical strain distribution around the entry: (**a**) concrete piles; (**b**) tube-piles; (**c**) filled piles.

The floor heave without reinforcement and after anti-shear pile installation at the second simulation step is shown in Figure 12. Figure 12 shows the floor uplift along the entry span for the maximum and minimum diameters of each studied pile type. Floor heave data were obtained from the model at 21 control points on the floor contour. The null point corresponds to the left leg of the steel arch frame. OX coordinates of the control points are shown in Figure 12 in the table. After the piles installation, the floor uplift decreases. Floor heave asymmetry along the entry span also significantly reduces. Concrete piles show the least effect in reducing both floor heave magnitude and asymmetry. Filled piles show the greatest effect. The maximal uplifts are observed not at the center of the entry span, but between points 11–13, between piles. Moreover, the decrease in floor height magnitude after floor reinforcement is accompanied by a shift in the maximum floor uplift toward the center of the entry span. For all pile types, a consistent decrease in floor uplift is observed with increasing pile diameter. Graphs of maximum floor uplift versus pile diameter are shown in Figure 13.



Point	OX, m	Point	OX, m	Point	OX, m	Point	OX, m
1	0.00	7	1.50	13	4.00	19	5.50
2	0.25	8	1.75	14	4.25	20	5.75
3	0.50	9	2.00	15	4.50	21	6.00
4	0.75	10	2.50	16	4.75		
5	1.00	11	3.00	17	5.00		
6	1.25	12	3.50	18	5.25		

Figure 12. Floor heave in gob-side entry without reinforcement and after pile installation.

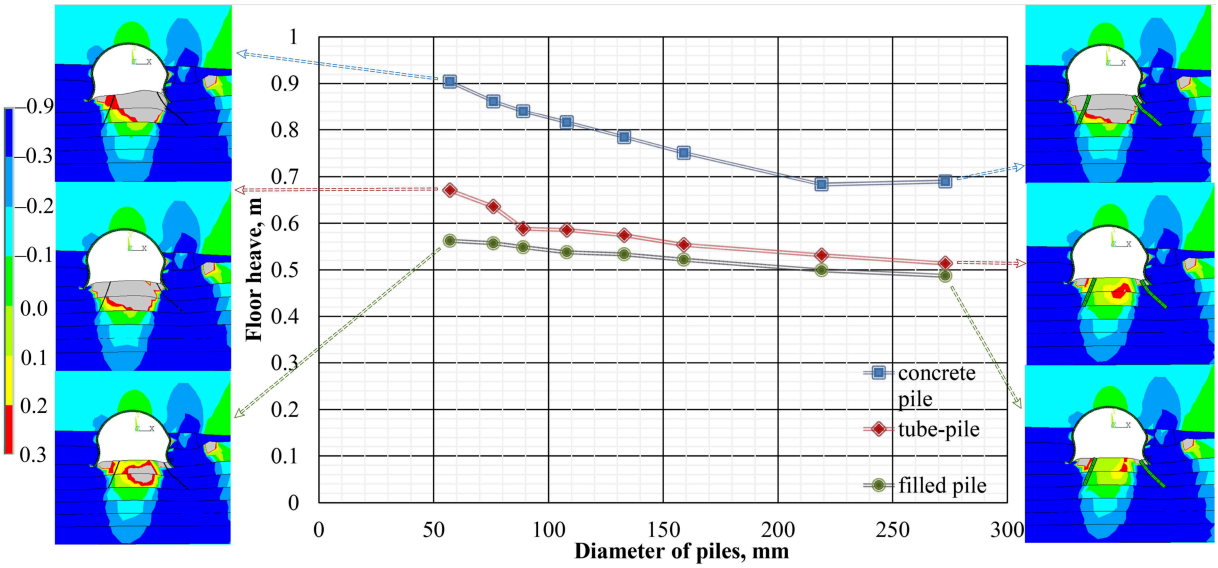


Figure 13. The relation between maximal floor heave and diameter of piles accompanied by vertical strain distribution around the entry for min and max pile diameter.

The floor uplift is the most sensitive to diameter variation for the case of concrete piles. Piles with a diameter of 57 mm had zero effect on floor uplift, while piles with a diameter of 273 mm reduced uplift by 24.1%. Tube piles with a diameter of 57–273 mm reduced floor uplift by 25.5–43%, respectively. In other words, the increase in pile diameter from minimum to maximum reduces floor uplift by 17.5%. Floor uplift is the least sensitive to diameter variation for the case of filled piles. With a 57 mm pile diameter, floor heave is reduced by 37.5%, while with a 273 mm diameter, it is reduced by 45.9%. This means that the variation in floor uplift is only 8.4%. Thus, concrete piles are the least efficient, but the floor heave is the most sensitive to variation in their diameter. Filled piles, on the other hand, are more efficient, but changes in their diameter do not significantly affect the floor heave.

Figure 13 shows that the reduction in floor uplift due to floor reinforcement occurs simultaneously with a reduction in the zone of vertical post-peak strains in the floor. Figure 14 shows the change in strain in the immediate floor. Strain data were obtained from the model at 31 control points in the immediate floor. Null point corresponds to the entry's contour. The OY coordinates of the control points are shown in Figure 14 in the table. The depth of pile influence is limited by the reinforcement depth, i.e., 2.0 m. However, concrete piles with a diameter of 57 mm do not change the nature of the strain distribution in the reinforcement zone, but merely reduce its amplitude. The uniform increase in strains toward the entry's contour is maintained as in the case without floor reinforcement. In all other cases, the opposite of the described trend is observed. In the near-contour zone, reinforcement causes a strain decrease. The core, where horizontal compression and vertical expansion occur, is located at a depth of 0.5–1.5 m. Analysis shows that only for tube-piles and filled piles with a diameter of 273 mm, both vertical and horizontal strains are in the pre-peak strain zone, as their magnitudes are less than the strain limit. This indicates a low risk of immediate floor failure, which corresponds with the analysis of strain distribution patterns in the entry's floor. Thus, effective control of floor heaves can be achieved either by increasing the diameter of the tube-pile and filled pile or by the installation of additional rock bolts in the expansion core to restrict delamination. A summary of the obtained results and a comprehensive analysis allow us to conclude that filled piles are the most effective in floor heave control.

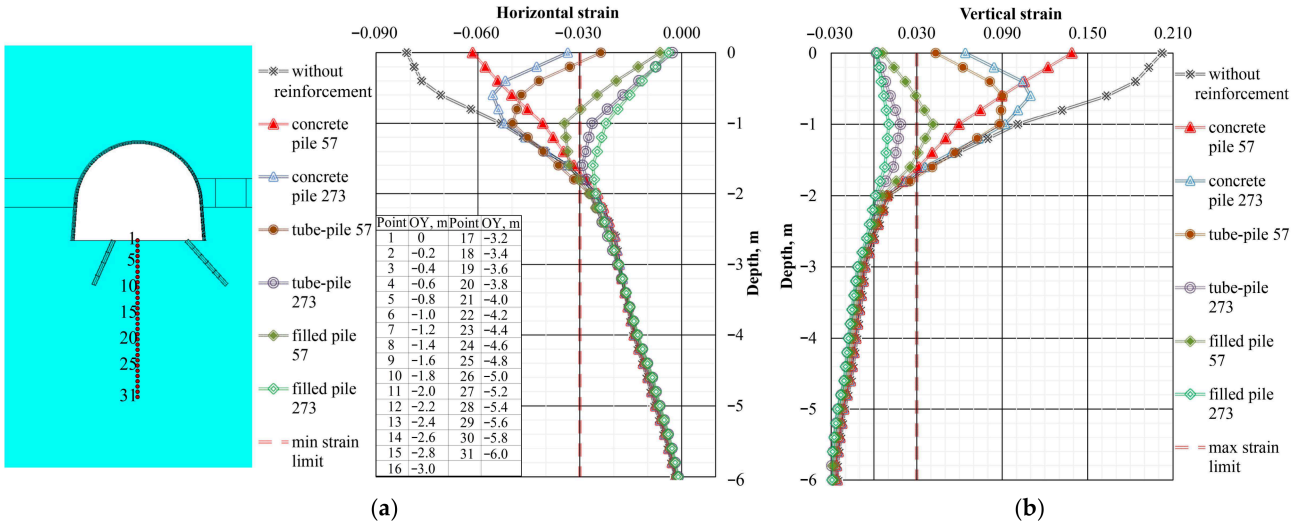


Figure 14. The variation in horizontal (**a**) and vertical (**b**) strains with depth.

5.3. Third Simulation Step

Figure 15 shows the floor heave without reinforcement and after installation of concrete piles and filled piles with different elastic moduli. The diameter of the piles was 133 mm. Concrete piles can crack over time. Different types of concrete and varying degrees of failure result in different elastic modulus values. The elastic modulus of cracked concrete was calculated in accordance with the Hoek-Brown Failure Criterion [45] using the method described above. For filled piles, the elastic modulus of pile material varied between 3 GPa and 200 GPa. This covered the entire range of possible pile rigidity. The general trend is towards decreasing floor asymmetry with increasing elastic modulus.

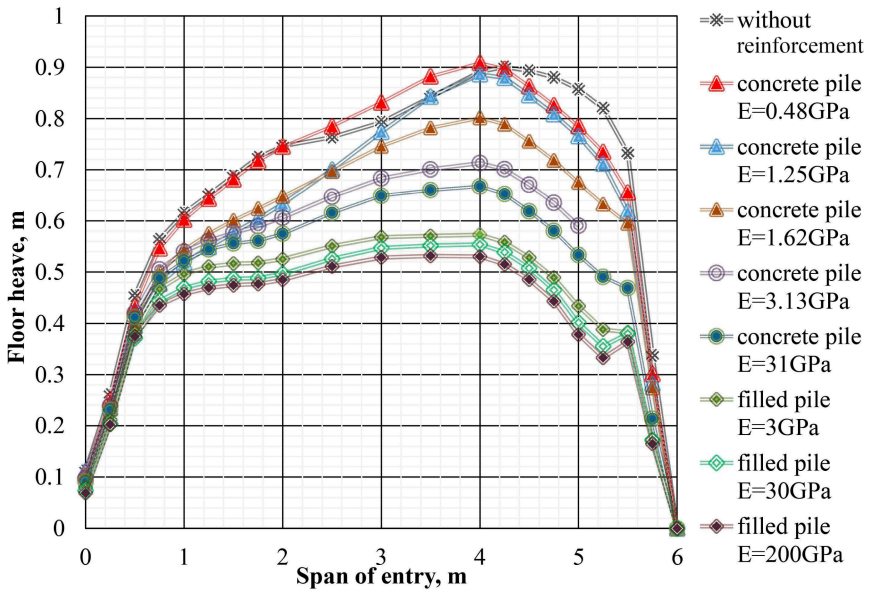


Figure 15. Floor heave in gob-side entry without reinforcement and after pile installation for different pile rigidity.

Different deformation models for concrete piles (the Drucker-Prager model) and filled piles (the bilinear isotropic hardening model) give different results with the same elastic modulus. Filled piles are more effective in floor heave control, likely due to the presence of a steel tube encasing the concrete, which prevents it from failure. Thus, with an elastic modulus of 3 GPa, concrete piles reduce floor uplift by 21%, and filled piles by 36%. With

an elastic modulus of 30 GPa, concrete piles reduce floor uplift by 27%, and filled piles by 39%. Figure 16 shows the floor heave after installation of concrete piles and filled piles with different elastic moduli. The zone of vertical post-peak strain consistently decreases with increasing elastic modulus of the pile material. The size of the post-peak vertical strain zone for filled piles with identical elastic moduli is significantly smaller. This can be seen in Figure 16, where the arrows show the vertical strain distribution patterns for elastic modulus of 3 and 30 GPa.

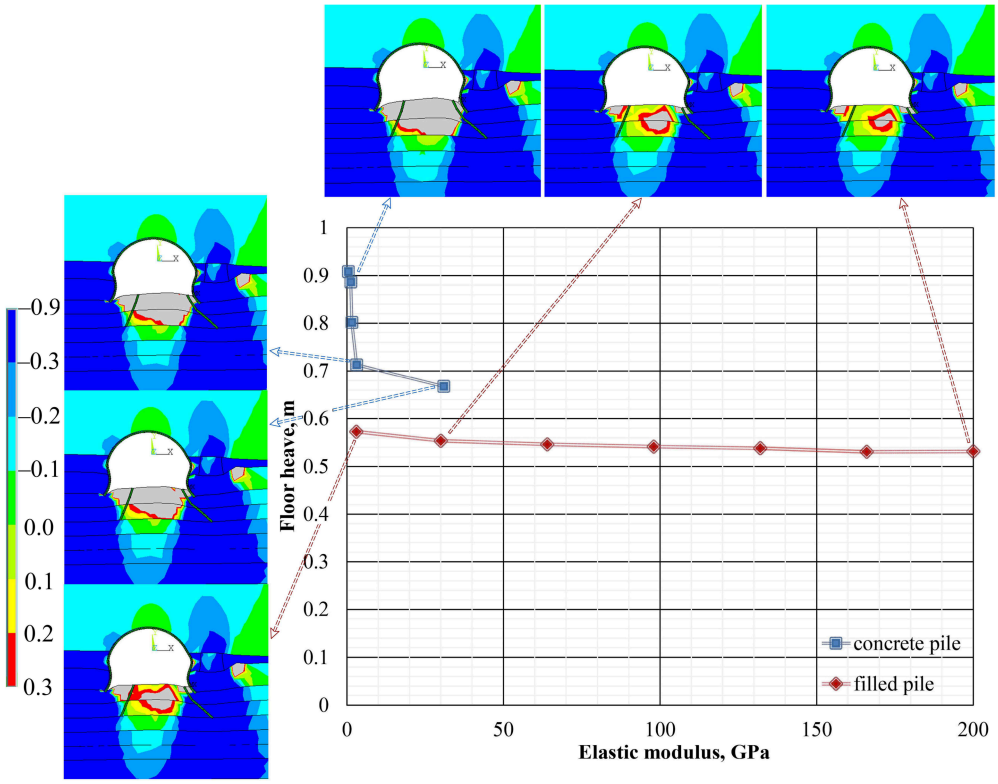


Figure 16. The relation between maximal floor heave and elastic modulus of piles accompanied by vertical strain distribution around the entry.

Figure 17 shows the variation in the vertical and horizontal strains in the immediate floor after installation of concrete piles and filled piles with different elastic moduli. The installation of piles changes the character of the strains in the near-contour zone. Unlike the case without reinforcement, the strain maximum is not located at the entry's contour, but at a depth of 0.5–1.0 m. The increase in pile elastic modulus leads to a shift in the strain maximum in the immediate floor. For concrete piles with the lowest elastic modulus, the strain maximum is at a depth of 0.4 m, while for concrete piles with the highest modulus, it is at a depth of 1.0 m. For filled piles with the lowest elastic modulus, the strain maximum is at a depth of 1.0 m, while for filled piles with the highest modulus, it is at a depth of 1.6 m. Moreover, only in the case of filled piles with an elastic modulus of 200 GPa, vertical strain in the entry's floor was lower than the strain limit. Generally, filled piles are more effective than other types of piles in both floor control and strain reduction in the immediate floor.

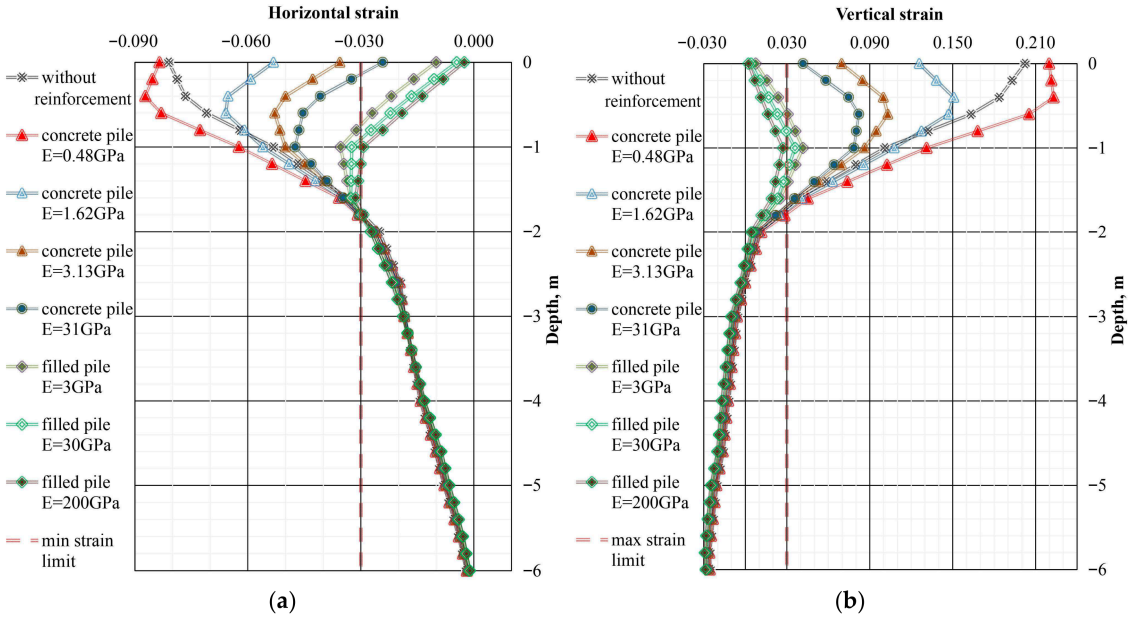


Figure 17. The variation in horizontal (**a**) and vertical (**b**) strains with depth.

6. Discussion

The main results of the conducted analysis are:

(1) In the side walls of the gob-side entry, the increased compressive vertical stresses are formed. The surrounding rocks are in an asymmetrical stress–strain field. The zone of increased stress in the roof from the coal body side is larger than the zone of increased stress from the filling wall side. Below the filling wall, vertical stress is higher than on the side of the coal seam body, and the depth of the post-peak strain zone is 2.5 times greater. The high vertical stresses and high vertical compressive strains below the filling wall and coal body transform into high horizontal stresses and strains below the support legs and subsequently transform into vertical tensile strains below the entry span. Restriction of the above-mentioned transformations in the immediate floor is an effective way to control the floor heave.

(2) The installation of anti-shear piles leads to a decrease in the floor heave and a reduction in its asymmetry. Concrete piles show the least effect, and filled piles show the greatest effect on the mentioned values. For all pile types, the increase in pile diameter leads to a decrease in floor uplift.

Concrete piles are the least efficient ones, but the floor heave is the most sensitive to variation in their diameter. Filled piles, on the other hand, are more efficient, but changes in their diameter do not significantly affect the floor heave. The greatest vertical delamination of the immediate floor occurs between the piles, at a depth of 0.5–1.5 m. The less floor uplift, the deeper the core of horizontal compression and vertical expansion is located. Effective control of floor heave can be achieved either by increasing the diameter of the piles or by the installation of additional rock bolts in the zone of maximal immediate floor expansion to restrict delamination. This study does not discuss the installation of additional rock bolts. Since with an increase in pile diameter, the cost of floor heave control method and the labor intensity of the work become significantly greater, it is proposed to look for ways to improve the effectiveness of anti-shear piles by increasing their rigidity and load-bearing capacity.

(3) The increase in the elastic modulus of pile material leads to a decrease in the floor heave, reducing its asymmetry, and a decrease in the size of the post-peak strain zone in the immediate floor. Since it is impossible to change the elastic modulus of

steel tube-piles, its effect on this type of pile has not been studied. Filled piles are more effective at floor heave control, likely due to the steel tube encasing the concrete, which prevents the concrete from failure. For example, at an elastic modulus of 3 GPa and 30 GPa, filled piles are 1.71 and 1.44 times more effective at decreasing floor uplift than concrete piles.

Thus, it can be concluded that the factors that have the highest impact on the effectiveness of the floor heave control method for the 2-pile 5 + 2 pile installation scheme are the pile's elastic modulus and its deformation mode. Filled piles (steel tubes filled with concrete) are the most effective ones since they show elastic behavior under high loads. The steel tube prevents the concrete from failing under loads. At the same time, the concrete inside the tube increases the steel tube's resistance to deformation. No significant increase in the effectiveness of filled piles has been observed with increasing diameter. Therefore, it makes sense to look for reserves of load-bearing capacity in the pile design. The main requirement for piles is maximal rigidity and load-bearing capacity with a minimal diameter. Since the materials used in filled piles have consistent properties, studies on improving pile design have high potential. The authors will conduct further research in this area.

7. Conclusions

This study is focused on improving the anti-shear pile floor heave control method in gob-side entry retaining. The main research method was numerical finite element modeling in ANSYS 17.2 software. The most effective type of anti-shear piles was found. The influence of pile diameter and its rigidity on the efficiency of floor heave control was determined. Based on the results of this study, the following conclusions can be drawn:

(1) In gob-side entry, retaining the asymmetry of the floor heave is caused by the indenting of the filling wall into the entry floor, resulting in a non-uniform stress–strain field in the immediate floor. The maximum floor heave is shifted along the entry span from its center toward the filling wall. Pile installation restricts the transformation of high vertical stresses and high vertical compressive strains in the sides of the entry into high horizontal stresses and strains below the frame support legs, and a subsequent transformation into vertical tensile strains below the entry span. The asymmetrical pile installation scheme is caused by the asymmetrical nature of the floor heave.

(2) Concrete piles show the least effect in reducing floor heave magnitude, asymmetry of floor uplift, and size of post-peak strain in the immediate floor. Filled piles show the greatest effect. For all pile types the increase in pile diameter leads to a decrease in floor uplift. The floor uplift is the most sensitive to diameter variation for the case of concrete piles, and the least sensitive for the case of filled piles. The increase in pile diameter from 57 mm to 273 mm leads to a decrease in floor uplift by 0–24.1%, 25.5–43%, and 37.5–45.9% for concrete piles, tube-piles, and filled piles, respectively. Filled piles are more efficient, but changes in their diameter do not significantly affect the floor heave. The search of further improvement of the effectiveness of anti-shear piles should be carried out in the direction of increasing the rigidity and load-bearing capacity of piles.

(3) An increase in the elastic modulus of the pile material leads to a decrease in the floor heave, reduction in its asymmetry, and a decrease in the size of the post-peak strain zone in the immediate floor. The different deformation modes of concrete piles and filled piles determine their different load-bearing capacities and the continuity of the pile material under load. In filled piles, the steel tube prevents the concrete core from fracturing, while the concrete core prevents the steel tube from plastic yielding. With the same elastic moduli of 3 GPa and 30 GPa, concrete piles reduce floor heave by 21% and 27%, while filled piles reduce it by 36% and 39%, respectively. Therefore, the

most impactful factors affecting the effectiveness of the floor-heave control are the pile's elastic modulus and pile deformation mode.

(4) The main requirements for piles that can be formulated based on the research results are maximum rigidity and load-bearing capacity with a minimum diameter. It would be more appropriate to focus future research on the improvement of pile design. The authors will conduct further research in this area.

Author Contributions: Conceptualization, I.S. and S.S.; methodology, L.S., O.K. and I.S.; software, I.S., O.K. and S.S.; validation, O.K.; formal analysis, S.B., O.K., D.D. and L.S.; investigation, I.S.; resources, S.B., L.S. and O.N.; data curation, S.S., O.N. and S.B.; writing—original draft I.S. and O.K.; writing—review and editing, I.S., S.S., S.B., D.D., L.S. and O.N.; visualization, L.S. and S.S.; super-vision, I.S.; project administration, I.S.; funding acquisition, O.K., D.D. and O.N. All authors have read and agreed to the published version of the manuscript.

Funding: This research received no external funding.

Institutional Review Board Statement: Not applicable.

Informed Consent Statement: Not applicable.

Data Availability Statement: The original contributions presented in this study are included in the article. Further inquiries can be directed to the corresponding author.

Acknowledgments: The authors are grateful to the administration of Technical University "Metinvest Polytechnic" LLC for supporting this research.

Conflicts of Interest: The authors declare no conflicts of interest.

References

1. He, M.; Song, S.; Wang, Q.; Yang, H.; Qi, H.; Guo, Z. Theory of longwall mining by using roof cuting shortwall team and 110 method—The third mining science and technology reform. *Coal Sci. Technol. Mag.* **2017**, *1*, 1–9+13. [CrossRef]
2. Hu, J.; He, M.; Wang, J.; Ma, Z.; Wang, Y.; Zhang, X. Key Parameters of Roof Cutting of Gob-Side Entry Retaining in a Deep Inclined Thick Coal Seam with Hard Roof. *Energies* **2019**, *12*, 934. [CrossRef]
3. He, M.; Wang, Q.; Wu, Q. Innovation and future of mining rock mechanics. *J. Rock. Mech. Geotech. Eng.* **2021**, *13*, 1–21. [CrossRef]
4. Wang, M.; Xu, Y.L.; Xu, Q.Y.; Shan, C.F.; Li, Z.H.; Nan, H.; Li, Y.F.; Liu, H.L.; Chu, T.X. Stability control of overburden and coal pillars in the gob-side entry under dynamic pressure. *Int. J. Rock. Mech. Min. Sci.* **2023**, *170*, 105490. [CrossRef]
5. Xie, S.R.; Wang, E.; Chen, D.D.; Li, H.; Jiang, Z.S.; Yang, H.Z. Stability analysis and control technology of gob-side entry retaining with double roadways by filling with high-water material in gently inclined coal seam. *Int. J. Coal Sci. Technol.* **2022**, *9*, 52. [CrossRef]
6. Kong, D.; Pu, S.; Cheng, Z.; Wu, G.; Liu, Y. Coordinated Deformation Mechanism of the Top Coal and Filling Body of Gob-Side Entry Retaining in a Fully Mechanized Caving Face. *Int. J. Geomech.* **2021**, *21*, 04021030. [CrossRef]
7. Sakhno, I.; Sakhno, S.; Kamenets, V. Stress environment around head entries with pillarless gobside entry retaining through numerical simulation incorporating the two type of filling wall. *IOP Conf. Ser. Earth Env. Sci.* **2022**, *1049*, 012011. [CrossRef]
8. Hao, J.; Zhang, P.; Song, Y.; Liu, H.; Shi, Y.; Liu, J.; Lu, G. Research on Pillarless Mining by Gob-Side Caving under Soft Rock Roof Conditions: A Case Study. *Appl. Sci.* **2023**, *13*, 2816. [CrossRef]
9. Sakhno, I.; Sakhno, S.; Isaienkov, O.; Kurdiumow, D. Laboratory studies of a high strength roof bolting by means of self-extending mixtures. *Min. Miner. Depos.* **2019**, *13*, 17–26. [CrossRef]
10. Faria Santos, C.; Bieniawski, Z.T. Floor design in underground coal mines. *Rock. Mech. Rock. Eng.* **1989**, *632*, 249–271. [CrossRef]
11. Gong, P.; Ma, Z.; Ni, X.; Zhang, R.R. Floor heave mechanism of gob-side entry retaining with fully-mechanized backfilling mining. *Energies* **2017**, *10*, 2085. [CrossRef]
12. Li, Z.; Zhang, Y.; Ma, Q.; Zheng, Y.; Song, G.; Yan, W.; Zhang, Y.; Hu, L. The floor heave mechanism and control technology of gob-side entry retaining of soft rock floor. *Sustainability* **2023**, *15*, 6074. [CrossRef]
13. Yu, G.; Wang, J.; Hu, J.; Zhu, D.; Sun, H.; Ma, X.; Ming, W.; Li, W. Innovative control technique for the floor heave in goaf-side entry retaining based on pressure relief by roof cutting. *Math. Probl. Eng.* **2021**, *2021*, 7163598. [CrossRef]
14. Lin, D.; Wei, X.; Chunzhao, X.U.; Tang, B. Research on the type and deformation mechanism of floor heave of swelling soft rock roadway along goaf in deep mine. *Min. Res. Dev.* **2013**, *33*, 23–26.

15. Sun, X.M.; Chen, F.; He, M.C.; Gong, W.L.; Xu, H.C.; Lu, H. Physical modeling of floor heave for the deep-buried roadway excavated in ten degree inclined strata using infrared thermal imaging technology. *Tunn. Undergr. Space Technol.* **2017**, *63*, 228–243. [CrossRef]
16. Małkowski, P.; Ostrowski, Ł.; Stasica, J. Modeling of floor heave in underground roadways in dry and waterlogged conditions. *Energies* **2022**, *15*, 4340. [CrossRef]
17. Guo, G.; Kang, H.; Qian, D.; Gao, F.; Wang, Y. Mechanism for Controlling Floor Heave of Mining Roadways Using Reinforcing Roof and Sidewalls in Underground Coal Mine. *Sustainability* **2018**, *10*, 1413. [CrossRef]
18. Kang, Y.; Liu, Q.; Gong, G.; Wang, H. Application of a combined support system to the weak floor reinforcement in deep underground coal mine. *Int. J. Rock. Mech. Min. Sci.* **2014**, *71*, 143–150. [CrossRef]
19. Zhang, Z.Y.; Shimada, H. Numerical study on the effectiveness of grouting reinforcement on the large heaving floor of the deep retained goaf-side gateroad: A case study in China. *Energies* **2018**, *11*, 1001. [CrossRef]
20. Mo, S.; Ramandi, H.L.; Oh, J.; Masoumi, H.; Canbulat, I.; Hebblewhite, B.; Saydam, S. A new coal mine floor rating system and its application to assess the potential of floor heave. *Int. J. Rock. Mech. Min.* **2020**, *128*, 104241. [CrossRef]
21. Yu, F.; Yang, J.; Zhou, K.; Liu, B. Mechanism and control measures for floor heave in gob-side entry of weakly cemented soft rock. *Sci. Rep.* **2025**, *15*, 33578. [CrossRef]
22. Chen, A.; Sun, Q.; Wang, X. Relief-Retaining Control Technology of Floor Heave in Mining Roadways. *Chin. J. Rock. Mech. Eng.* **2021**, *40*, 349–360. [CrossRef]
23. Liu, H.; Liu, C.; Zhai, M.; Zhang, P.; Wang, L.; Wang, F.; Liu, J. Collaborative Control Technology of Crosscut Floor Heave in Soft Rocks under Deep High Horizontal Stress. *Math. Probl. Eng.* **2022**, *2022*, e8260169. [CrossRef]
24. Wang, D.; Zheng, Y.; He, F.; Song, J.; Zhang, J.; Wu, Y.; Jia, P.; Wang, X.; Liu, B.; Wang, F.; et al. Mechanism and Control of Asymmetric Floor Heave in the Gob-Side Coal Roadway under Mining Pressure in Extra-Thick Coal Seams. *Energies* **2023**, *16*, 4948. [CrossRef]
25. Yuping, F.; Yiming, R.; Yongliang, H.; Li, C. Mechanism and control technology of roadway floor heave deformation and failure under the influence of repeated mining in multiple coal seams. *Sci. Rep.* **2025**, *15*, 31415. [CrossRef]
26. Gai, Q.; He, M.; Li, S.; Gao, Y. Study on Strike Failure Characteristics of Floor in a New Type of Pillarless Gob-side Entry RetainingTechnology Above Confined Water. *Tunn. Undergr. Space Technol.* **2025**, *161*, 106596. [CrossRef]
27. Qin, Q.; Guan, W.; Ji, F.; Wang, H.; He, M. Sensitivity Analysis of Coal-Pillar Loading and Roadway Floor Heave in High-Intensity Longwall Mining: Implications for Pressure-Relief Design. *Symmetry* **2026**, *18*, 286. [CrossRef]
28. Sakhno, I.; Sakhno, S.; Skrzypkowski, K.; Isaienkov, O.; Zagórski, K.; Zagórska, A. Floor Heave Control in Gob-Side Entry Retaining by Pillarless Coal Mining with Anti-Shear Pile Technology. *Appl. Sci.* **2024**, *14*, 4992. [CrossRef]
29. Xu, Y.; Chen, J.; Bai, J. Control of floor heaves with steel pile ingob-side entry retaining. *Int. J. Min. Sci. Technol.* **2016**, *26*, 527–534. [CrossRef]
30. Kang, X.; Guo, D.; Lu, Z. Mechanism of roadway floor heave controlled by floor corner pile in deep roadway underhigh horizontal stress. *Adv. Civ. Eng.* **2021**, *2021*, 6669233. [CrossRef]
31. Guo, D.; Kang, X.; Lu, Z.; Chen, Q. Mechanism and Control of Roadway Floor Rock Burst Induced by High Horizontal Stress. *Shock Vib.* **2021**, *2021*, 6745930. [CrossRef]
32. Ma, H.; Zhang, S.; Zhai, H.; Liu, Z.; Jie, C. Numerical Simulation and Engineering Application of Synergistic Support Effect of Bolt–Mesh–Cable Support in Gob-Side Entry of Deep Soft Coal Seam. *Appl. Sci.* **2024**, *14*, 8226. [CrossRef]
33. Tian, Z.; Dong, L.; Liu, Y. Numerical Simulation Analysis on Deformation Mechanism of Shallow-Buried Soft Rock Roadway. *Adv. Mater. Res.* **2023**, *734–737*, 773–776. [CrossRef]
34. He, B.; Yin, G.Z. Stability analysis of tunnel during the excavation based on ANSYS. *Appl. Mech. Mater.* **2014**, *577*, 1135–1138. [CrossRef]
35. Bondarenko, V.; Kovalevska, I.; Brovko, D.; Shyshov, M.; Kozii, Y.; Snihur, M.; Poimanov, S. Substantiation of resource-saving technologies for supporting and protecting mine workings at their repeated use. *Min. Miner. Depos.* **2026**, *20*, 90–104. [CrossRef]
36. Bondarenko, V.; Sheka, I.; Khorolskyi, A.; Salieiev, I.; Kovalevska, I.; Stoliarska, O. Substantiation of rational parameters for composite support in mine workings. *Nauk. Visnyk Natsionalnoho Hirnychoho Universytetu* **2025**, *3*, 58–64. [CrossRef]
37. Sakhno, I.; Sakhno, S. Control of floor heave with rock bolts-steel piles coupling support technology. *Int. J. Coal Sci. Technol.* **2026**, *13*, 44. [CrossRef]
38. Ma, M.; Guo, Q.; Pan, J.; Ma, C.; Cai, M. Optimal Support Solution for a Soft Rock Roadway Based on the Drucker–Prager Yield Criteria. *Minerals* **2022**, *12*, 1. [CrossRef]
39. Dai, N.; Geng, D.; Yuan, J.; Zhai, G.; Chen, Y. A new Drucker–Prager model considering material softening effects. *Eng. Comput.* **2025**, *42*, 3803–3825. [CrossRef]
40. Wang, X.; Wei, Y.; Jiang, T.; Hao, F.; Xu, H. Elastic–plastic criterion solution of deep roadway surrounding rock based on intermediate principal stress and Drucker–Prager criterion. *Energy Sci. Eng.* **2024**, *12*, 2472–2492. [CrossRef]

41. Wang, R.; Liu, X.; Bai, J.; Yan, S.; Xu, J. An Innovative Elastoplastic Analysis for Soft Surrounding Rock considering Supporting Opportunity Based on Drucker-Prager Strength Criterion. *Adv. Civ. Eng.* **2021**, *2021*, 5555839. [CrossRef]
42. Chen, L.; Mao, X.-B.; Li, M.; Chen, Y.-L. Elastoplastic analysis of cracked surrounding rock in deep roadway based on Drucker–Prager criterion. *J. China Coal Soc.* **2017**, *42*, 484–491. [CrossRef]
43. Zhang, X.b.; Zhao, G.-m.; Meng, X.-r. Elastoplastic solution for surrounding rock of circular roadway based on DP criterion by considering post-peak strain softening and dilatancy. *J. Min. Saf. Eng.* **2013**, *30*, 903–910.
44. Gong, H.; Li, D.; Luo, P.; Ru, W.; Zhang, G.; Liu, Y. Influence of advance direction on surrounding rock stability of main ramp under deep high ground stress. *Eng. Fail. Anal.* **2024**, *161*, 108309. [CrossRef]
45. Hoek, E.; Carranza-Torres, C.; Corkum, B. Hoek-Brown failure criterion—2002 edition. In Proceedings of the 5th North American Rock Mechanics Symposium and the 17th Tunnelling Association of Canada Conference, NARMS-TAC, Toronto, ON, Canada, 7–10 July 2002; pp. 267–271.
46. Hoek, E.; Diederichs, M. Empirical estimates of rock mass modulus. *Int. J. Rock. Mech. Min. Sci.* **2006**, *43*, 203–215. [CrossRef]
47. Bieniawski, Z.T. *Engineering Rock Mass Classifications*; Wiley: New York, NY, USA, 1989.
48. *DSTU 8943:2019*; Ukrainian Scientific Research and Training Center of Standardization; Certification and Quality Problems (UkrNDNC). Electric-Welded Steel Pipes. Specifications. UkrNDNC: Kyiv, Ukraine, 2019.
49. Zhou, H.; Zhang, C.; Li, Z.; Hu, D.; Hou, J. Analysis of mechanical behavior of soft rocks and stability control in deep tunnels. *J. Rock. Mech. Geotech. Eng.* **2014**, *6*, 219–226. [CrossRef]
50. Almisned, O.A.; Alqahtani, N. Rock analysis to characterize Saudi soft sandstone rock. *J. Petrol. Explor. Prod. Technol.* **2021**, *11*, 2381–2387. [CrossRef]
51. Liu, Q.; Liang, B.; Sun, W.; Zhao, H. Experimental study on the difference of shale mechanical properties. *Adv. Civ. Eng.* **2021**, *2021*, 6677992. [CrossRef]

Disclaimer/Publisher's Note: The statements, opinions and data contained in all publications are solely those of the individual author(s) and contributor(s) and not of MDPI and/or the editor(s). MDPI and/or the editor(s) disclaim responsibility for any injury to people or property resulting from any ideas, methods, instructions or products referred to in the content.